

Submitted to The Astrophysical Journal

MAGNETICALLY ARRESTED DISKS AND ORIGIN OF POYNTING JETS: NUMERICAL STUDY

Igor V. Igumenshchev

*Laboratory for Laser Energetics, University of Rochester
250 East River Road, Rochester, NY 14623*

iigu@lle.rochester.edu

ABSTRACT

The dynamics and structure of accretion disks, which accumulate the vertical magnetic field in the centers, are investigated using two- and three-dimensional MHD simulations. The central field can be built up to the equipartition level and disrupts a nearly axisymmetric outer accretion disk inside a magnetospheric radius, forming a magnetically arrested disk (MAD). In the MAD, the mass accretes in a form of irregular dense spiral streams and the vertical field, split into separate bundles, penetrates through the disk plane in low-density magnetic islands. The accreting mass, when spiraling inward, drags the field and twists it around the axis of rotation, resulting in collimated Poynting jets in the polar directions. These jets are powered by the accretion flow with the efficiency up to $\sim 1.5\%$ (in units $\dot{M}_{in}c^2$). The spiral flow pattern in the MAD is dominated by modes with low azimuthal wavenumbers $m \sim 1 - 5$ and can be a source of quasi-periodic oscillations in the outgoing radiation. The formation of MAD and Poynting jets can naturally explain the observed changes of spectral states in Galactic black hole binaries. Our study is focused on black hole accretion flows; however, the results can also be applicable to accretion disks around nonrelativistic objects, such as young stellar objects and stars in binary systems.

Subject headings: accretion, accretion disks — black hole physics — galaxies: jets — gamma rays: bursts — instabilities — ISM: jets and outflows — magnetic fields — MHD — turbulence

1. Introduction

Accretion disks can carry small- and large-scale magnetic fields. The small-scale field ($\ell \lesssim R$, where ℓ is the field scale length and R measures the radial distance from the disk center) can be locally generated by the MHD dynamo (Brandenburg et al. 1995; Stone et al. 1996) supported by the turbulence, which results from the magneto-rotational instability (MRI, Balbus & Hawley 1991). This field can provide the outward transport of angular momentum in the bulk of the disk with the help of local Maxwell stresses (Shakura & Sunyaev 1973; Hawley, Gammie, & Balbus 1996). The large-scale field ($\ell > R$) is unlikely produced in accretion disks (however, see Tout & Pringle 1996), and can either be captured from the environment and dragged inward by an accretion flow (Bisnovatyi-Kogan & Ruzmaikin 1974, 1976), or inherited from the past evolution (see §4). The large-scale field can remove the angular momentum from accretion disks by global Maxwell stresses through the magnetized disk corona (Königl 1989).

A large-scale bipolar field, unlike a small-scale field, can not dissipate locally due to the magnetic diffusivity and can not be absorbed by the central black hole. In the case of inefficient outward diffusion of the bipolar field through the disk (see Narayan, Igumenshchev, & Abramowicz 2003; Spruit & Uzdensky 2005; Bisnovatyi-Kogan & Lovelace 2007; and for other possibility, see van Ballegooijen 1989; Lubow, Papaloizou, & Pringle 1994; Lovelace, Romanova, & Newman 1994; Heyvaerts, Priest, & Bardou 1996; Agapitou & Papaloizou 1996; Livio, Ogilvie, & Pringle 1999), this field is accumulated in the innermost region of an accretion disk and forms a “magnetically arrested disk,” or MAD (Narayan et al. 2003). The MAD consists of two parts: the outer, almost axisymmetric, Keplerian accretion disk and the inner magnetically dominated region, in which the accumulated vertical field disrupts the outer disk at the magnetospheric radius $R_m \sim 8\pi GM\rho/B^2$, where M is the central mass, ρ is the accretion mass density, and B is the magnetic induction.

It is believed that the large-scale bipolar field in accretion disks is responsible for the formation of jets observed in a large variety of astrophysical objects (e.g., Livio, Pringle, & King 2003). The magnetically driven jets can be of two types, basically depending on a mass load by the disk matter (e.g., Lovelace, Gandhi, & Romanova 2005): Poynting jets and hydromagnetic jets, which have, respectively, small and large mass loads. The hydromagnetic jets can be formed by two mechanisms: the magneto-centrifugal mechanism (Blandford & Payne 1982; Königl & Pudritz 2000) and the toroidal-field pressure generated by the disk rotation (Lynden-Bell 2003; Kato, Mineshige, & Shibata 2004). The magneto-centrifugal mechanism produces relatively wide outflows and, to be consistent with observations of the collimated jets, requires an additional focusing mechanism. Jets driven by the toroidal-field pressure can have a high degree of collimation, but these jets are known to be kink unstable

(Eichler 1993; Apel 1996; Spruit, Foglizzo, & Stehle 1997). Poynting jets are naturally self-collimated and expected to be marginally kink stable (Li 2000; Tomimatsu, Matsuoka, & Takahashi 2001). These jets can originate in the innermost region of accretion disks and powered either by the disks themselves (Lovelace, Wang, & Sulkanen 1987; Lovelace et al. 2002) or by rotating black holes (Blandford & Znajek 1977; Punsly 2001; also see, Takahashi et al. 1990; Komissarov 2005; Hawley & Krolik 2006; McKinney 2006).

Our study is based on two- and three-dimensional (2D and 3D, respectively) MHD simulations and has two main goals. First, we investigate the dynamics and structure of MAD’s. We show that MAD’s are formed in the accretion flows, which carry inward large-scale poloidal magnetic fields. Inside the magnetospheric radius R_m , the matter accretes as discrete streams and blobs, fighting its way through the strong vertical magnetic field fragmented in separate bundles. Because of rotation, the streams take spiral shapes. Second, we demonstrate a link between the existence of MAD’s and production of powerful Poynting jets. These jets should always be generated in MAD’s because of the interaction of the spiraling accretion flow with the vertical magnetic bundles, which, as the result, are twisted around the axis of rotation.

This paper extends the work of Igumenshchev, Narayan, & Abramowicz (2003) by studying in more detail the radiatively inefficient accretion disks with poloidal magnetic fields. We employ a new version of our 3D MHD code, which can be utilized in multi-processor simulations. The paper is organized as follows: We describe the solved equations, the numerical method used, and initial and boundary conditions in §2. We present our numerical results in §3, and discuss and summarize them in §4.

2. Numerical method

We simulate nonradiative accretion flows around a Schwarzschild black hole of mass M using the following equations of ideal MHD:

$$\rho \frac{d\rho}{dt} + \rho \nabla \cdot \mathbf{v} = 0, \quad (1)$$

$$\rho \frac{d\mathbf{v}}{dt} = -\nabla P - \rho \nabla \Phi + \frac{1}{4\pi} (\nabla \times \mathbf{B}) \times \mathbf{B}, \quad (2)$$

$$\frac{\partial}{\partial t} \left(\rho \frac{v^2}{2} + \rho \epsilon + \frac{B^2}{8\pi} + \Phi \right) = -\nabla \cdot \mathbf{q}, \quad (3)$$

$$\frac{\partial \mathbf{B}}{\partial t} = \nabla \times (\mathbf{v} \times \mathbf{B}), \quad (4)$$

where \mathbf{v} is the velocity, P is the gas pressure, Φ is the gravitational potential, ϵ is the specific internal energy of gas, and \mathbf{q} is the total energy flux per unit square (see, e.g., Landau & Lifshitz 1987). We adopt the ideal gas equation of state,

$$P = (\gamma - 1)\rho\epsilon, \quad (5)$$

with an adiabatic index $\gamma = 5/3$. We neglect self-gravity of the gas and employ a pseudo-Newtonian approximation (Paczyński & Wiita 1980) for the black hole potential

$$\Phi = -\frac{GM}{R - R_g}, \quad (6)$$

where $R_g = 2GM/c^2$ is the gravitational radius of the black hole. No explicit resistivity and viscosity are applied in equations (2)-(4). However, because of the use of the total energy equation (3), the energy released due to the numerical resistivity and viscosity is consistently accounted as heat in our simulations.

The MHD equations (1)-(4) are solved employing the time-explicit Eulerian finite-difference method, which is an extension to MHD of the hydrodynamic piecewise-parabolic method by Colella & Woodward (1984). We solve the induction equation (4) using the constrained transport (Evans & Hawley 1988; Gardiner & Stone 2005), which preserves the $\nabla \cdot \mathbf{B} = 0$ condition. In our method, we employ the approximate MHD Riemann solver by Li (2005). Test simulations have shown that this solver is robust and provides a good material interface tracking.

We use the spherical coordinates (R, θ, ϕ) . Our 3D numerical grid has $182 \times 84 \times 240$ zones in the radial, polar, and azimuthal directions, respectively. The radial zones are spaced logarithmically from $R_{in} = 2R_g$ to $R_{out} = 220R_g$. Both hemispheres are considered, in which polar cones with the opening angle $\pi/8$ are excluded. Therefore, the polar domain extends from $\theta = \pi/16$ to $15\pi/16$. The grid resolution in the polar direction is gradually changed from a fine resolution around the equatorial plane to a coarse resolution near the poles (with the maximum-to-minimum grid-size ratio ≈ 3). The azimuthal zones are uniform and cover the full 2π range in ϕ . The absorption condition for the mass and the condition of the zero-transverse magnetic field are applied in the inner and outer radial boundaries, providing that the mass and field can freely leave the computational domain through these boundaries. In the boundaries around the excluded polar regions, we apply the reflection boundary conditions, which means that no streamlines and magnetic lines can go through these boundaries.

At the beginning of our simulations, the computational domain is filled with a very low-density, nonmagnetized material. The simulations are started in 2D, assuming the axial

symmetry, with an injection of mass in a slender torus, which is located in the equatorial plane at $R_{inj} = 210 R_g$; i.e., close enough to R_{out} . This mass has the Keplerian angular momentum and specific internal energy $\epsilon_{inj} = 0.045 GM/R_{inj}$. After an initial period of simulation without magnetic fields, the mass forms a steady thick torus, which has the inner edge at $R \approx 150 R_g$ and which outer half is truncated at R_{out} . The torus contains a constant amount of mass and is in a dynamic equilibrium: all the injected mass flows outward through R_{out} after a circulation inside the torus. No accretion flow at this point is formed. This hydrodynamic, steady, thick torus is used as an initial configuration in our MHD simulations.

The MHD simulations are started at $t = 0$ from the steady, thick torus by initiating the injection of a poloidal magnetic field into the injection slender torus at R_{inj} . The numerical procedure for the field injection is similar to that described by Igumenshchev et al. (2003) except for one modification: now the strength of the injected field can be limited by setting the minimum β_{inj} , which is the ratio of the gas pressure to the magnetic pressure at R_{inj} . This modification allows us to better control the rate of field injection. The entire volume of the thick torus is filled by the field during about one orbital period, t_{orb} , estimated at R_{inj} . Since this moment, $t \simeq t_{orb}$, the formation of accretion flow begins as a result of redistribution of the angular momentum in the torus due to Maxwell stresses. In the following discussion, we will use the time normalized by the time-scale t_{orb} , i.e. $t \rightarrow t/t_{orb}$.

3. Results

We present the results of combined axisymmetric 2D and non-axisymmetric 3D simulations. The initial evolution in our models has been simulated in 2D. This allows us to consider longer evolution times in comparison to those that can be obtained in 3D simulations, because of the larger requirements for computational resources in the latter case. We initiate 3D simulations starting from developed axisymmetric models. The results have shown that non-axisymmetric motions are not very important in the outer parts of the constructed accretion flows and, therefore, the use of 2D simulations on the initial evolution stages is the reasonable simplification.

We consider three models, which differ by the rates of field injection determined by $\beta_{inj} = 10, 100$, and 1000 , and we will refer to these models as Model A, B, and C, respectively. All other properties of the models, including the injection radius R_{inj} , internal energy ϵ_{inj} , and numerical resolution, are the same (see §2).

3.1. Accretion flows

The initial axisymmetric development of the models is qualitatively similar: the inner edge of the thick torus is extended toward the black hole, forming relatively thin, almost Keplerian accretion disks. The time of the disk development is varied, depending on the strength of the injected field. The accretion of the mass into the black hole begins at $t \approx 0.7$ in Model A, ≈ 1.3 in Model B, and ≈ 4.2 in Model C (time is given in units of the orbital period at R_{inj} , see §2). At this stage, the evolution of the disks is governed mainly by global Maxwell stresses produced by the poloidal field component. This component is advected inward with the accretion flow and, because of the disks' Keplerian rotation, generates relatively strong toroidal magnetic fields localized above and below the mid-plane. These toroidal fields form a highly magnetized disk corona with a typical $\beta \sim 0.01$. Model B and, especially Model C, demonstrate the development of 2D MRI. This development is similar to that observed by Stone & Pringle (2001); in particular, in their “Run C.” We have found the origin of the channel solution (see Hawley & Balbus 1992) in the central regions of Models B and C. This solution consists of oppositely directed radial streams and is the characteristic feature of the axisymmetric non-linear MRI (Stone & Norman 1994). Analysis of the models shows that the channel solution is developed when the wavelength $\lambda = 2\pi V_A / \sqrt{3}\Omega$ of the fastest growing mode of the MRI is well resolved on the numerical grid, i.e. $\lambda \gtrsim 5\Delta x$, where Δx is the grid size, V_A is the Alfvén velocity, and Ω is the angular velocity. Model A shows no indication of the MRI, which can be attributed to the strong magnetic fields, which suppress the instability. In this model, the estimate of λ typically exceeds the disk thickness. Model A has some resemblance to nonturbulent “Run F” of Stone & Pringle (2001). In spite of the mentioned similarities with the results of Stone & Pringle (2001), our models show different behavior on the long evolution times. Our simulation design with the permanent injection of mass and magnetic field results in accretion disks, which accumulate the poloidal field in the center and form MAD's. The models of Stone & Pringle (2001; also De Villiers, Hawley, & Krolik 2003; Hirose et al. 2004; McKinney & Gammie 2004; Hawley & Krolik 2006) did not form MAD's and did not show a long-time accretion history, probably because of the initiation of simulations from static magnetized tori, which contain a limited amount of mass and magnetic flux of one sign. We will concentrate on the results describing the formation, evolution, and structure of MAD's in the following text. Other aspects of our results will be reported elsewhere.

Figure 1 shows example snapshots of the axisymmetric density distribution in Model B from 2D simulations at two successive moments, $t = 5.1153$ and 5.1458 . The accretion flow is nonuniform because of the development of turbulence. The turbulence results from the combined effect of the MRI and current sheet instability. The latter instability locally releases heat due to reconnections of the oppositely directed toroidal magnetic fields. The

reconnection heat makes a significant contribution to the local energy balance in the central regions of the flow, because of the relatively high energy density of the field, which is comparable to the gravitational energy density of the accretion mass. The thick disk structure observed in Fig. 1 is explained by convection motions supported by the reconnection heat. Note that the case, in which the turbulence is supported by only convection motions from the reconnections, without the effects of rotation and MRI, had been demonstrated in simulations of spherical magnetized accretion flows (Igumenshchev 2006). In the case of disk accretion, almost axisymmetric convection motions, similar to those found here, had been observed in 3D models with toroidal magnetic fields (Igumenshchev et al. 2003). The convection motions in Models B and C make these models relevant to convection-dominated accretion flows (Narayan, Igumenshchev, & Abramowicz 2000; Quataert & Gruzinov 2000). Our simulations show that the poloidal field is transported inward in axisymmetric turbulent flows and accumulated in the vicinity of the black holes. When the central poloidal field reaches some certain strength (about equipartition with the gravitational energy of the accreting mass), the accretion flow becomes unstable (Narayan et al. 2003). In axisymmetric simulations, the instability takes the form of cycle accretion, in which the more-extended periods of halted accretion (see Fig. 1a) are followed by the relatively short periods of accretion (see Fig. 1b). In the case of the halted accretion period, the inner accretion disk is truncated at the magnetospheric radius R_m , which is $\approx 15 R_g$ in Fig. 1a. The pressure of the strong central vertical field (see Fig. 2a) prevents the mass accumulated at R_m from falling into the black hole. The accretion begins as soon as the gravity of the accumulated mass overcomes the magnetic pressure. During the accretion period, the whole magnetic flux, which is localized inside R_m in the period of halted accretion, is moved on the black hole horizon (see Fig. 2b). Note that similar structural features of the inner MHD flows in accretion disks related to the model of gamma-ray bursts were discussed by Proga & Zhang (2006).

Figure 3 illustrates the time dependence of the accretion flow in Model B, showing the evolution of the mass accretion rate \dot{M}_{in} and magnetic fluxes in the midplane inside the five specific radii: $210 R_g$ ($= R_{inj}$), $100 R_g$, $50 R_g$, $25 R_g$, and $2 R_g$ ($= R_{inj}$). This figure shows the evolution, which has been simulated in 2D from $t = 0$ to 2.14 and in 3D after $t = 2.14$. The vertical dashed line in Fig. 3 indicates the moment of initiation of the 3D simulations. The cycle accretion in the 2D simulations begins at $t \approx 1.4$ and is clearly seen as a sequence of spikes in the time-dependence of \dot{M}_{in} (see Fig. 3a). Spikes, which are related to the same cycle accretion, are also observed in the variation of magnetic flux inside $R = 2 R_g$ (see Fig. 3b). The magnetic fluxes inside the other selected radii are gradually increased with time because of the inward advection of the vertical field. The time dependence of these fluxes is not significantly influenced by the cycle accretion.

The structure and dynamics of the inner region in Model B are drastically changed in the 3D simulations. Shortly after the initiation of the 3D simulations at $t = 2.14$, the axisymmetric distribution of mass near R_m undergoes the Rayleigh-Taylor and, possibly, Kelvin-Helmholtz instability (see Kaisig, Tajima, & Lovelace 1992; Spruit, Stehle, & Papaloizou 1995; Chandran 2001; Li & Narayan 2004) with the fastest growing azimuthal mode number $m \simeq 50$ (the latter is probably determined by our grid resolution). As a result, the empty region inside R_m is quickly filled, on the free-fall time scale estimated at R_m , with the large number of density spikes moved almost radially toward the center. These spikes quickly disappear in the black hole and, at a later time, the inner disk structure is modified toward establishing a dynamic quasi-steady state. This state is characterized by a low m -mode ($m \simeq 1-5$) spiral-flow structure, which results from the interaction of the accreting mass with the strong vertical magnetic field. Note that the similar low m -mode flow structure was found in the simulations of accretion flows onto a magnetic dipole (Romanova & Lovelace 2006).

The non-axisymmetric inner flow is highly time-variable and experiences a quasi-periodic behavior. Figure 4 shows an example of the flow structure inside $50 R_g$ in Model B, at two successive moments: $t = 2.2767$ and 2.2867 . The flow is essentially 3D inside the magnetically dominated region limited by the radius $\simeq 35 R_g$ and remains almost axisymmetric on the outside of this radius. In the magnetically dominated region, the flow forms moderately tightened spirals of dense matter, which are clearly seen in Figs 4a and 4b. This matter is quickly accreted into the black hole with the radial velocity, which is ~ 0.5 a fraction of the free-fall velocity. Such a relatively fast infall is explained by the efficient loss of the angular momentum by the mass during its interaction with the vertical field. The field is distributed nonuniformly in the disk plane, concentrating in bundles that penetrate through the plane in very low density, magnetically dominated (with $\beta \sim 0.01$) regions, or magnetic “islands.” The rotating mass interacts with magnetic bundles and forces them to twist around the disk’s rotational axis. In the simulations, this twist is observed as the rotation of magnetic islands around the center in the disk plane. The rotational velocity of the islands typically has the reduced rotational velocity by the factor of $\sim 0.5-1$ in comparison with the velocity of the surrounding accretion matter. This can be explained by the resistance of the large-scale vertical field to such a twist. The faster rotation of accretion matter and slower rotation of magnetic islands produces a shear flow. The shear flow plays two roles in our simulations. First, it provides the exchange of momentum and energy between the accreting mass and vertical field. Second, the shear flow results in an ablation of the islands caused by magnetic diffusivity, making each island a temporal structure. An example evolution of magnetic islands can be seen in Fig. 4: the magnetic islands observed as low-density spiral arms above the center in Fig. 4a are observed below the center in Fig. 4b, after about half a

revolution in the clockwise direction. In the latter figure, the islands are apparently reduced in size due to the ablation.

The vertical field ablated from magnetic islands is carried inward by the accretion flow and accumulates on the black hole horizon. This accumulation results in quasi-periodic eruptions of the field outward from the horizon as soon as the field pressure overcomes the dynamic pressure of the accreting mass. The eruptions typically take the form of high-velocity narrow streams (in the equatorial cross-section) of a low-density, magnetically dominated medium fountained outward from the black hole. In Fig. 4b, four magnetic islands observed as low-density regions inside $R \approx 15 R_g$ result from such eruptions and the eruption of one of these islands (to the right from the center; see also the steam that produced it) still continues at the moment shown. In the consequent evolution, these islands are pushed outward and stretched in the azimuthal direction by the accretion flow, and take the spiral shape similar to that shown in Fig. 4a.

Model A evolves faster and accumulates a larger magnetic flux at the center in comparison with Model B. Figure 5 shows the evolution of the accretion rate \dot{M}_{in} and magnetic fluxes in Model A. Qualitatively, the evolution of these quantities is similar to the evolution of those in Model B (see Fig. 3). Quantitatively, however, Model A demonstrates significantly larger time-averaged accretion rates (by about two orders of magnitude) and longer quasi-periods of the cycle accretion (represented by the intervals between spikes in the time-dependence of \dot{M}_{in} in Fig. 5a) in the 2D simulations. By the end of the 2D simulations at $t \approx 1.7$, this model has the maximum $R_m \simeq 30 - 40 R_g$.

In the 3D simulations, Model A experiences the initial transient period, similar to the period of the development of the Rayleigh-Taylor instability in Model B (see above), in which the non-axisymmetric, small-scale structures quickly appear and disappear. Figure 6 shows an example of the developed low m -mode spiral structure in Model A obtained after the transient period. This structure is clearly dominated by the $m = 1$ mode. The magnetically dominated region is extended up to $R \simeq 70 R_g$. Note that the spiral-density arms seen in Fig. 6 are more open than the arms in Model B (see Fig. 4a). This could be due to the stronger central field in Model A.

Model C is our slowest evolving model and, accordingly, shows the slowest rate of accumulation of the central vertical field. This model has been calculated only in 2D and demonstrated the qualitative similarity to the axisymmetric evolution of Models A and B. The cycle accretion, which is caused by the accumulated field, begins at $t \approx 4.8$ in Model C. The model demonstrates more-efficient turbulent motions in the accretion flow. This can be attributed to weaker magnetic fields, which suppress less the MRI and convection motions. At the end of simulation at $t \approx 6$, the model has the maximum $R_m \simeq 6 R_g$.

3.2. Poynting Jets

The 3D simulations of Models A and B show that the vertical field penetrated the central magnetically dominated regions in MAD's is twisted around the axis of rotation by the rotating accretion flows. The field twist generates electromagnetic perturbations, which propagate outward and transport the released energy in the form of a Poynting flux (e.g., Landau & Lifshitz 1987)

$$\mathbf{S} = \frac{1}{8\pi}((\mathbf{v} \times \mathbf{B}) \times \mathbf{B}). \quad (7)$$

The Poynting flux is distributed nonuniformly in the polar angles, basically showing two components: a jet-like concentration of the flux near the poles and a wide-spread distribution of the flux in the equatorial and mid-polar-angle directions (from $\theta \sim \pi/4$ to $\sim 3\pi/4$).

Figures 7 and 8 show example θ -distributions of the radial Poynting flux (solid lines),

$$S_R = v_R \frac{B^2}{4\pi} - \frac{B_R}{4\pi}(\mathbf{v} \cdot \mathbf{B}), \quad (8)$$

at six different radii, $5 R_g$, $10 R_g$, $25 R_g$, $50 R_g$, $100 R_g$, and $220 R_g$, which cover most of the radial domain in Models B and A, respectively. The shown distributions are averaged in the azimuthal direction and in time over the interval $\Delta t \simeq 0.05$, using a set of data files stored during the simulations. Outside of the inner magnetically dominated region (at $R \gtrsim 35 R_g$ in Model B and $R \gtrsim 70 R_g$ in Model A), the outward (positive) Poynting flux in the equatorial and mid-polar-angle directions is supported mostly by the rotation of the outer, almost axisymmetric disks, in which the poloidal field component is frozen in. Such a flux is present in both the axisymmetric 2D and 3D simulations. The 3D simulations introduce new important features in the Poynting flux distribution: an increase of the flux at the equatorial and mid-polar-angle directions inside the magnetically dominated region, and at the polar directions outside this region (see Figs 7 and 8). The equatorial flux inside the magnetically dominated region is generated due to the twist of the vertical field by the spiraling non-axisymmetric accretion flows. In Model B, this flux, represented by bumps in the θ -distributions, gradually deviates from the equatorial plane toward the poles as the radial distance increases (see Figs 7a-7d). At $R \gtrsim 100 R_g$, the flux is collimated into bi-polar Poynting jets (see Figs 7e and 7f). In the case of Model A, the process of jet collimation is less evident and somewhat different; but still, one can observe the formation of narrow bi-polar Poynting jets starting from $R \simeq 10 R_g$ and further development of these jets at large radii (see Figs 8b-8f).

Figures 7 and 8 show θ -distributions of the kinetic flux (dashed lines),

$$F_R = v_R \rho \frac{v^2}{2}, \quad (9)$$

for comparison with the Poynting flux. Typically, the kinetic flux is comparable, but does not exceed the Poynting flux in the polar jets (except in the outermost region in Model A, see Fig.8f). Accordingly, the jet velocity is mostly sub-Alfvénic. However, the value of the kinetic flux is relatively large and this is in some contradiction with our expectations that MAD’s can develop Poynting flux dominated jets. The problem of the excessive kinetic flux in our simulations can probably be explained by the action of the numerical magnetic diffusivity (see §4), which results in an unphysically large mass load of the Poynting jets and the consequent excessive kinetic flux in them.

The Poynting jets are powered by the released binding energy of the accretion mass. To estimate quantitatively the amount of energy going into the jets, we calculate the Poynting jet “luminosity” \dot{E}_{jet} as a function of the radius R ,

$$\dot{E}_{jet}(R) = \int R^2 S_R d\Omega, \quad (10)$$

where the integration is taken over the solid angles Ω occupying the polar regions with $\theta < \pi/4$ and $\theta > 3\pi/4$ (excluding the boundary polar cones, see §2). For comparison, we also calculate the Poynting total luminosity \dot{E}_{tot} , which is defined analogously to \dot{E}_{jet} , but with the integration in eq. (9) taken over the whole sphere. Figures 9 and 10 show the radial profiles of the normalized \dot{E}_{jet} (solid lines) and \dot{E}_{tot} (dashed lines) in Models B and A, respectively. The jet luminosity \dot{E}_{jet} weakly depends on the radius at $R \gtrsim 50 R_g$ in both models and equals to $\approx 1.5\%$ in Model B and $\approx 0.5\%$ in Model A. Here, we quantify the luminosity in the units of accretion power $\dot{M}_{in}c^2$. The total luminosity \dot{E}_{tot} includes the flux from the bi-polar Poynting jets and wide equatorial Poynting outflow. The latter component of \dot{E}_{tot} exceeds \dot{E}_{jet} by the factor of ~ 3 at large radii (see Figs 9 and 10). This can be the consequence of the employed simulation design (see §2), in which the disk accretion at outer radii is mostly provided by the global Maxwell stresses.

The smaller value of the final (at large radii) relative \dot{E}_{jet} in Model A, in comparison with that in Model B, can be explained by the different structure of the inner magnetically dominated region in these models. Model A has the less tighten spiral density arms (see Fig. 6), in which the mass accretes with larger radial velocity and, therefore, delivers less energy to the field. Note, also, that the value of \dot{E}_{jet} in Model A takes the relatively large finite value right at the inner boundary R_{in} (see Fig. 10), whereas \dot{E}_{jet} in Model B begins from a small value at R_{in} and gradually increases outward (see Fig. 9). This difference in the behavior of \dot{E}_{jet} can be attributed to the discussed difference of the innermost structure in the considered models.

4. Discussion and Conclusions

We have performed a numerical study of the formation and evolution of quasi-stationary MAD, which is characterized by a strong vertical magnetic field accumulated at the disk center. We employ the simulation design, in which the poloidal magnetic field of one sign is permanently injected into the computational domain at the outer numerical boundary and the unipolar vertical field is transported inward by the accretion flow. The accumulated field has a significant impact on the inner flow structure and dynamics in both 2D and 3D simulations. In the axisymmetric 2D simulations, the field pressure can temporarily halt the mass falling into the black hole, resulting in the cycle accretion, in which the longer periods of accumulation of the mass at the magnetospheric radius R_m are followed by the short periods of accretion. The 3D simulations have shown, however, that the axisymmetric cycle accretion is not realized. Instead, the accumulated field causes the mass to accrete quasi-regularly in the form of non-axisymmetric spiral streams and blobs. We have demonstrated that 3D MAD's can be efficient sources of collimated, bipolar Poynting jets, which originate in the vicinity of the central black hole. These jets develop due to and are powered by the interaction of the spiral mass inflows with the central field split into separate magnetic bundles. The efficiency of conversion of the accretion energy $\dot{M}_{in}c^2$ into the Poynting jet energy is up to 1.5% in our simulations. This estimate may not be accurate (we believe, underestimated) because of the use of the pseudo-Newtonian approximation (see §2). The better estimate of the efficiency can be obtained using general relativistic MHD simulations.

We have presented the simulation results from three models of radiatively inefficient accretion disks, which differ by the strength of the injected field. In accordance with the previous studies (e.g., Stone & Pringle 2001), the structure of the outer disks in these models is determined by the field strength. In Model A, which has the largest injected field, the MRI is suppressed and the accretion flow is driven by global Maxwell stresses, which transport the excessive angular momentum outward from the disk through the disk corona. In Models B and C, which have the smaller injected fields, the MRI and turbulent motions are developed. The turbulence in these models is axisymmetric and partially supported by the efficient convection motions resulting from dissipation of toroidal and small-scale, poloidal magnetic fields. These motions cause the increase of the disk thicknesses in comparison with non-turbulent Model A. The 3D simulations of Models A and B have demonstrated that non-axisymmetric motions are not important in the outer parts of the disks, outside the inner magnetically dominated region (the disks remain almost axisymmetric), but very important inside this region, resulting in the development of the spiral accretion flows and bi-polar Poynting jets.

Numerical magnetic dissipations and reconnections result in a magnetic diffusivity,

which influences the structure and dynamics of our models. The spatial scale, on which the diffusivity occurs in our simulations, is determined by the gridsize, which greatly exceeds the scales of various resistive mechanisms (e.g., Coulomb collisions, dissipative plasma instabilities) in the relevant astrophysical conditions. Therefore, the magnetic diffusivity is significantly overestimated in our models and results in an excessive slippage of an accretion flow through magnetic field. This slippage reduces the ability of the flow to drug inward the vertical field, but, however, the numerical diffusivity is not efficient enough to totally prevent the field accumulation at the disk center. The numerical diffusivity suppresses the MRI on the scales of the gridsize, and, therefore, prevents the development of turbulence in the outer regions of our models, where the gridsize is increased. Other effect of the numerical magnetic diffusivity is the enhancement of the ablation of magnetic islands, which are found in the 3D simulations (see §3.1). To test the sensitivity of our models to magnetic dissipations, we have performed a 2D simulation of the model, which is similar to Model A, but has the double number of grid points in the R - and θ -directions. The simulation has demonstrated the qualitative similarity of axisymmetric evolution of the high resolution model and Model A: both models show the formation of accretion disks, accumulation of the vertical field in the disk centers, and development of the cycle accretion. The high resolution model forms a thinner laminar accretion disk. Unfortunately, a more detailed quantitative comparison of these models meets some difficulties because of the different properties of the mass and field injection region (see §2), which are changed with the change of the resolution.

The main results of our study, the formation of MAD's and Poynting jets, have been obtained under the assumption of radiatively inefficient flows, but, we believe that these results can also be applied to the radiatively efficient, dense accretion disks (e.g., Kato, Fukue, & Mineshige 1998). The formation of MAD's should not be affected by the radiative cooling as soon as the central field satisfies the equipartition condition,

$$\frac{B^2}{8\pi} \sim \frac{GM\rho}{R_g}, \quad (11)$$

where ρ is the mass density in the innermost region. The radiative losses results in the higher ρ and, therefore, the larger B is necessary to obtain radiative MAD's. We expect that the qualitatively similar spiral structure of the inner magnetically dominated region, to that found in our simulations, can be developed in the case of the radiative disks. Poynting jets should be a necessary attribute of the radiative MAD's as well.

The formation of MAD's in the radiative disks can be used to explain the observations of the low/hard state in black hole binaries (for a review, see Remillard & McClintock 2006). Here, we briefly discuss basic moments of this application of MAD's and leave more quantitative considerations for future works. We assume, for example, the development of

the MAD in the radiation pressure dominated accretion disk at the subcritical regime (see Shakura & Sunyaev 1973). In such a disk, the radiation diffusion time scale $t_{rad} \simeq H^2 \sigma_T \rho / c$ can significantly exceed the Keplerian time $t_K = 2\pi R^{3/2} / \sqrt{GM}$ at small values of the α -parameter, $\alpha \lesssim 0.1$, in virtue of the relation

$$\frac{t_K}{t_{rad}} \simeq 3.4\alpha, \quad (12)$$

which follows from the Shakura-Sunyaev solution. Here, we denote H to be the disk half-thickness and $\sigma_T = 0.4 \text{ cm}^2/\text{g}$ to be the Thomson scattering cross-section. As soon as $t_{rad} \gg t_K$ in the outer Shakura-Sunyaev disk, t_{rad} can also significantly exceed the accretion velocity $t_{accr} \sim t_K$ in the inner spiral flow in the MAD, in virtue of the relation

$$\frac{t_{accr}}{t_{rad}} \propto R, \quad (13)$$

which is satisfied in accretion flows with the scaling law of the accretion velocity $v_{accr} \propto R^{-1/2}$ and $H \propto R$. Having $t_{rad} \gg t_{accr}$, one concludes that the radiation is trapped inside the spiral flow on the accretion time scale and, therefore, this flow is radiatively inefficient. From the point of view of an observer, which detects the softer part of the spectrum of outgoing radiation (below $\sim \text{eVs}$), the MAD will look like a Shakura-Sunyaev disk truncated at the inner radius R_{tr} , which coincides with the transition radius between the inner magnetically dominated region and outer axisymmetric accretion disk. Typically, in observations, R_{tr} is in the interval from a few tens to hundreds of R_g (e.g., in Cyg X-1, see Done & Zycki 1999), which is consistent with that obtained in our Models A and B. The observed spectra of black hole binaries in the low/hard state are dominated by the hard x-ray component (e.g., Done, Gierliński, & Kubota 2007) and this can be explained by the radiation from the hot, optically thin magnetized medium, which surrounds the accreting spiral flows and in which the binding energy of these flows is released. The synchrotron radiation from the magnetized medium and Poynting jets in the MAD (see Goldston, Quataert, & Igumenshchev 2005) can be used to explain the observed radio luminosity in the low/hard state; this luminosity is believed to be due to steady jets (e.g., Corbel et al. 2003; Gallo, Fender, & Pooley 2003).

Our simulations assume accretion disks around black holes and can be relevant to objects with relativistic jets containing accreting stellar-mass black holes (e.g., in micro-quasars; black holes resulted from type Ib/c supernova explosions and mergers of two compact objects) and supermassive black holes (in galactic centers). However, we believe that our main results can also be relevant to nonrelativistic astrophysical objects, in which accretion disks and jets are observed. These objects include, for example, young stellar objects and accreting stars (e.g., white dwarfs) in binary systems. Qualitatively, we expect that the structure and dynamics of MAD's and Poynting jets are similar in the both relativistic and nonrelativistic

cases. We expect, however, large quantitative differences in these two cases because of the different energy-density scales involved in the regions of jet formation. Black holes, which are capable of launching jets almost from the event horizon, can produce ultra relativistic jets (e.g., McKinney 2006). Jets from nonrelativistic objects, which have the surface radius $R_* \gg R_g$, are limited by the velocities $v \sim \sqrt{GM/R_*} \ll c$. For example, the latter formula gives the upper estimate of the jet velocity $\sim 400 \text{ km/s}$ from the solar-type stars.

The problem of inward transport and amplification of the vertical field in turbulent accretion disks was intensively discussed in past and recent years (see, e.g., Spruit & Uzdensky 2005). The solution of this problem can help to discriminate models of accretion disks, which are consistent with observations (e.g., Meier & Nakamura 2006; Schild, Leiter, & Robertson 2006). Our simulation results show that the vertical field is transported inward and amplified independent of the disk structure, either laminar or turbulent. It is worth noting, however, that magnetic fields in our models are imposed and relatively large. The assumed strength of these fields exceeds the possible strength of the self-sustained magnetic fields that could be developed due to the MRI (Sano et al. 2004). Therefore, these results should be considered with some caution, because they do not represent the case of weak vertical magnetic fields.

The strong vertical field in the center of accretion disks can be, in principal, a relic field that is inherited from the previous evolution. This field can appear, for example, in the merger scenario (merger of two magnetized neutron stars or a black hole with a magnetized neutron star, e.g., Berger et al. 2005) or in the course of the gravitational collapse of an extended “proto” object (e.g., proto-stellar cloud, supernova progenitor), which produces a significantly more compact object (protostar, black hole). In the latter case, the proto object may contain some amount of the poloidal field, which will be amplified and accumulated at the center during the collapse. After the formation of the compact object, the remained noncollapsed mass can still move inward, forming an accretion disk and confining the field in the vicinity of the object. Depending on the relative strength of this relic field and the mass accretion rate, MAD’s and Poynting jets can be developed. The considered scenario can be applied to young stellar objects (T-Tauri stars, e.g., Donati et al. 2007) and the hyper-accretion model for gamma-ray bursts (Woosley 1993; Paczyński 1998).

The spiral-flow pattern in MAD’s rotates with about the same angular velocity at all radial distances; i.e., it rotates almost as a rigid body. Such a rotation can result in quasi-periodic oscillations (QPO’s) in the emitted radiation, if the disk’s axis is inclined to the line of view of an observer (e.g., Alpar & Shaham 1985; Lamb et al. 1985; Strohmayer et al. 1996; Lamb & Miller 2001; Titarchuk 2003). The frequency of these QPO’s should be related to the rotation of the spiral pattern, which angular velocity is defined by the radius of the magnetically dominated region and can be a fraction ($\sim 0.5 - 1$) of the orbital velocity at

this radius. More investigations are required to make quantitative predictions about QPO's from MAD's.

This work was supported by the U.S. Department of Energy (DOE) Office of Inertial Confinement Fusion under Cooperative Agreement No. DE-FC52-92SF19460, the University of Rochester, the New York State Energy Research and Development Authority.

REFERENCES

Agapitou, V., & Papaloizou, J.C.B. 1996, *Astrophys. Lett. Commun.*, 34, 363

Alpar, M. A., & Shaham, J. 1985, *Nature*, 316, 239

Appl, S. 1996, *A&A*, 314, 995

Balbus, S. A., & Hawley, J. F. 1991, *ApJ*, 376, 214

Berger, E. et al. 2005, *Nature*, 438, 988

Bisnovatyi-Kogan, G. S., & Ruzmaikin, A. A. 1974, *Ap&SS*, 28, 45

Bisnovatyi-Kogan, G. S., & Ruzmaikin, A. A. 1976, *Ap&SS*, 42, 401

Bisnovatyi-Kogan, G. S., & Lovelace, R. V. E. 2007, *ApJ*, 667, L167

Blandford, R.D., & Znajek, R.L. 1977, *MNRAS*, 179, 433

Blandford, R.D., & Payne, D.G. 1982, *MNRAS*, 199, 883

Brandenburg, A., Nordlund, A., Stein, R.F., & Torkelsson, U. 1995, *ApJ*, 446, 741

Cabral, B., & Leedom, L. 1993, *Computer Graphics: Proceedings: Annual Conference Series 1993: SIGGRAPH 93* (New York: Association for Computing Machinery), 263

Chandran, B. D. G. 2001, *ApJ*, 562, 737

Colella, P., & Woodward, P.R. 1984, *J. Comp. Phys.*, 54, 174

Corbel, S., Nowak, M. A., Fender, R. P., Tzioumis, A. K., & Markoff, S. 2003, *Astron. Astrophys.*, 400, 1007

De Villiers J.-P., Hawley, J. F., & Krolik, J. H. 2003, *ApJ*, 599, 1238

Donati, J.-F., Jardine, M. M., Gregory S. G., Petit, P., Bouvier, J., Dougados, C., Ménard, F., Cameron, A. C., Harries, T. J., Jeffers, S. V., & Paletou, F. 2007, *MNRAS*, 380, 1297

Done, C., & Zyczyński, P. T. 1999, *MNRAS*, 305, 457

Done, C., Gierliński, M., & Kubota, A. 2007, *Astron. Astrophys. Rev.*, in press

Eichler, D. 1993, *ApJ*, 419, 111

Evans, C.R., & Hawley, J.F. 1988, ApJ, 332, 659

Gallo, E., Fender, R. P., & Pooley, G. G. 2003, MNRAS, 344, 60

Gardiner, T.A., & Stone, J.M. 2005, J. Comp. Phys., 205, 509

Goldston, J. E., Quataert, E., & Igumenshchev, I. V. 2005, ApJ, 621, 785

Hawley, J. F., & Balbus, S. A. 1992, ApJ, 400, 595

Hawley, J.F., Gammie, C.F., & Balbus, S.A. 1996, ApJ, 464, 690

Hawley, J. F., & Krolik, J. H. 2006, ApJ, 641, 103

Heyvaerts, J., Priest, E.R., & Bardou, A. 1996, ApJ, 473, 403

Hirose, S., Krolik, J.H., De Villiers, J.-P., & Hawley, J.F. 2004, ApJ, 606, 1083

Igumenshchev, I. V. 2006, ApJ, 649, 361

Igumenshchev, I. V., Narayan, R., & Abramowicz, M. A. 2003, ApJ, 592, 1042

Kaisig, M., Tajima, T., & Lovelace, R. V. E. 1992, ApJ, 386, 83

Kato, S., Fukue, J., & Mineshige, S. 1998, Black-Hole Accretion Disks (Kyoto: Kyoto Univ. Press)

Kato, Y., Mineshige, S., & Shibata, K. 2004, ApJ, 605, 307

Komissarov, S.S. 2005, MNRAS, 359, 801

Königl, A. 1989, ApJ, 342, 208

Königl, A., & Pudritz, R. E. 2000, in Protostars and Planets IV, ed. V. Mannings, A. Boss, & S. Russell (Arizona: Univ. Arizona Press), p.759 (astro-ph/9903168)

Lamb, F. K., & Miller, M. C. 2001, ApJ, 554, 1210

Lamb, F. K., Shibasaki, N., Alpar, M. A., & Shaham, J. 1985, Nature, 317, 681

Landau, L. D., & Lifshitz, E. M. 1987, Electrodynamics of Continuous Media. Pergamon Press, Oxford

Li, L.-X. 2000, ApJ, 531, L111

Li, L.-X., & Narayan, R. 2004, ApJ, 601, 414

Li, S. 2005, J. Comp. Phys., 203, 344

Livio, M., Ogilvie, G.I., & Pringle, J.E. 1999, ApJ, 512, 100

Livio, M., Pringle, J.E., & King, A.R. 2003, ApJ, 593, 184

Lovelace, R. V. E., Wang, J. C. L., & Sulkanen, M. E. 1987, ApJ, 315, 504

Lovelace, R. V. E., Li, H., Koldoba, A. V., Ustyugova, G. V., & Romanova, M. M. 2002, ApJ, 572, 445

Lovelace, R. V. E., Gandhi, P. R., & Romanova, M. M. 2005, Ap&SS, 298, 115

Lovelace, R. V. E., Romanova, M. M., & Newman, W. I. 1994, ApJ, 437, 136

Lubow, S.H., Papaloizou, J.C.B., & Pringle, J.E. 1994, MNRAS, 267, 235

Lynden-Bell, D. 2003, MNRAS, 341, 1360

Meier, D.L., Nakamura, M. 2006, ASPC, 350, 195

McKinney, J. C., & Gammie, C. F. 2004, ApJ, 611, 977

McKinney, J. C. 2006, MNRAS, 368, 1561

Narayan, R., Igumenshchev, I. V., & Abramowicz, M. A. 2000, ApJ, 539, 798

Narayan, R., Igumenshchev, I. V., & Abramowicz, M. A. 2003, PASJ, 55, L69

Paczyński, B., & Wiita, P.J. 1980, A&A, 88, 23

Paczyński, B. 1998, ApJ, 494, L45

Proga, D., & Zhang, B. 2006, MNRAS, 370, L61

Punsly, B. 2001, Black Hole Gravitohydromagnetics (New York: Springer)

Quataert, E., & Gruzinov, A. 2000, ApJ, 539, 809

Remillard, R. A., & McClintock, J. E. 2006, Annu. Rev. Astron. Astrophys., 44, 49

Romanova, M. M., & Lovelace, R. V. E. 2006, ApJ, 645, L73

Sano, T., Inutsuka, S., Turner, N.J., Stone, J.M. 2004, ApJ, 605, 321

Schild, R.E., Leiter, D.J., & Robertson, S.L. 2006, AJ, 132, 420

Shakura, N. I., & Sunyaev, R.A. 1973, A&A, 24, 337

Spruit, H.C., Foglizzo, T., & Stehle, R. 1997, MNRAS, 288, 333

Spruit, H. C., Stehle, R., & Papaloizou, J. C. B. 1995, MNRAS, 275, 1223

Spruit, H.C., & Uzdensky, D.A. 2005, ApJ, 629, 960

Stone, J.M., Hawley, J.F., Gammie, C.F., & Balbus, S.A. 1996, ApJ, 463, 656

Stone, J. M., & Pringle, J. E. 2001, MNRAS, 322, 461

Stone, J. M., & Norman, M. L. 1994, ApJ, 433, 746

Strohmayer, T. E., Zhang, W., Swank, J. H., Smale, A., Titarchuk, L., Day, C., & Lee, U. 1996, ApJ, 469, L9

Takahashi, M., Nitta, S., Tatematsu, Y., & Tomimatsu, A. 1990, ApJ, 363, 206

Titarchuk, L. 2003, ApJ, 591, 354

Tomimatsu, A., Matsuoka, T., & Takahashi, M. 2001, Phys. Rev. D, 64, 123003

Tout, C. A., & Pringle, J. E. 1996, MNRAS, 281, 219

van Ballegooijen, A.A. 1989, in Proc. European Phys. Soc. Study Conf., Accretion Disks and Magnetic Fields in Astrophysics, ed. G. Belvedere (Dordrecht: Kluwer), 99

Woosley, S.E. 1993, ApJ, 405, 273

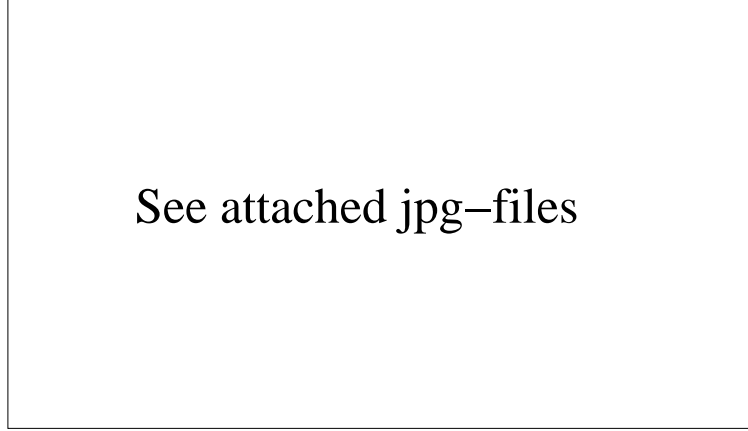


Fig. 1.— Distributions of density in the meridional plane in Model B at two successive moments (a) $t = 5.1153$ and (b) $t = 5.1458$ from axisymmetric 2D simulations. The black hole is located on the left and the small empty circle there corresponds to the inner boundary around the black hole at $R_{in} = 2 R_g$. The axis of rotation is in the vertical direction. The domain shown has the radial extent $100 R_g$ along the equatorial plane and represents a fraction of the full computational domain with $R_{out} = 220 R_g$. The time is in units of the orbital period at $R_{inj} = 210 R_g$. The color bars on the bottom indicate the scales for $\log \rho$ (in arbitrary units). The model develops the thick turbulent accretion disk, which is seen as the nonuniform mass concentration near the equator. The low-density polar regions are filled with the strong vertical magnetic field. This field causes the cycle accretion into the black hole. (a) The halted accretion period when the mass is accumulated at the magnetospheric radius $R_m \approx 15 R_g$ and (b) the accretion period.

Fig. 2.— Snapshot of magnetic lines in Model B at the same moments and on the same spatial scales as in Fig. 1. The component of the field lines parallel to the meridional plane is shown. The accretion disk transports the vertical magnetic flux inward, which accumulates in the vicinity of the black hole. Small-scale magnetic loops are the result of turbulent motions in the disk and disk corona. (a) The halted accretion period (see Fig. 1a), in which most of the accumulated magnetic flux is outside the black hole horizon. (b) The accretion period (see Fig. 1b), in which all the accumulated flux goes through the horizon. The lines have been plotted using the method of Cabral & Leedom (1993).

Fig. 3.— Evolution of mass accretion rate and magnetic fluxes in Model B. The time is in units of the orbital period at R_{inj} . The simulations are performed in 2D, assuming axisymmetry, from $t = 0$ to 2.14 (the latter moment indicated by the vertical dashed line) and in 3D after that. (a) The accretion into the black hole begins at $t \approx 1.3$. Starting from $t \approx 1.4$, the cycle accretion is developed (seen as a sequence of spikes). In 3D, the cycle accretion disappears. (b) Magnetic fluxes (in arbitrary units) through the equatorial plane inside five fixed radii: $2 R_g$ ($= R_{inj}$), $25 R_g$, $50 R_g$, $100 R_g$, and $210 R_g$ ($= R_{inj}$). The variability of the flux at R_{inj} is related to the variability of the accretion rate in (a).

Fig. 4.— Distributions of density in the equatorial plane in Model B at two successive moments (a) $t = 2.2767$ and (b) $t = 2.2867$ from 3D simulations. The black hole is located in the center and the central black circle corresponds to the inner boundary at $R_{in} = 2 R_g$. The shown domain has the extension 100 by $100 R_g$. The time is in units of the orbital period at $R_{inj} = 210 R_g$. The color bars on the bottom indicate the scales for $\log \rho$ (in arbitrary units). The accretion flow rotates in the clockwise direction and forms the spiral structure inside $R \approx 35 R_g$. The low-density regions correspond to the magnetically dominated islands, through which the vertical field penetrates the disk. (a) The developed structure of spiral density inflows and magnetic islands stretched in the azimuthal direction. (b) The moment after about half a revolution of the spiral magnetic pattern seen in (a); new magnetic islands inside $R \approx 15 R_g$ are the result of an eruption of the vertical magnetic flux from the inner boundary.

Fig. 5.— Evolution of mass accretion rate and magnetic fluxes in Model A. The notations used are the same as in Fig. 3. Note the earlier beginning of accretion, significantly larger accretion rate and magnetic fluxes, and longer quasi-periods between the accretion events in the 2D simulations in comparison with those in Model B (see Fig. 3). These are the result of a stronger field injection in Model A.

Fig. 6.— Distribution of density in the equatorial plane in Model A at $t = 1.82$ from 3D simulations. The notations used are the same as in Fig. 4. The shown domain has the extension 300 by $300 R_g$. The model is characterized by the relatively large magnetic flux accumulated at the center. The magnetically dominated region has the outer radius $R \simeq 70 R_g$. The accretion flow demonstrates the one-arm ($m = 1$ – mode) spiral structure in the innermost region. This structure rotates in the clock-wise direction and is split onto the three arms at larger radial distances. There are other two large density streams in the process of development (below the center and on the left from the center).

Fig. 7.— Distribution of Poynting S_R (solid lines) and kinetic F_R (dashed lines) radial fluxes in the θ -direction in Model B. The fluxes are averaged in the azimuthal direction and in time over the interval $\Delta t = 0.05$, beginning from $t = 2.27$, and normalized to the accretion power $\dot{M}_{in}c^2$. The distributions are shown at the radial distances $5 R_g$, $10 R_g$, $25 R_g$, $50 R_g$, $100 R_g$, and $220 R_g$ ($= R_{out}$) in the panels from (a) to (f), respectively, and illustrate the collimation of Poynting flux into bi-polar jets.

Fig. 8.— Same as in Fig. 7, but for Model A. The fluxes are averaged in time over the interval $\Delta t = 0.04$, beginning from $t = 1.78$.

Fig. 9.— Radial distribution of Poynting jet \dot{E}_{jet} (solid line) and total \dot{E}_{tot} (dashed line) luminosities in Model B. The luminosities are normalized to the accretion power $\dot{M}_{in}c^2$ and averaged in time as explained in the caption to Fig.7.

Fig. 10.— Same as in Fig. 9, but for Model A. The luminosities are averaged in time as explained in the caption to Fig.8.

This figure "fig1a.jpg" is available in "jpg" format from:

<http://arXiv.org/ps/0711.4391v1>

This figure "fig1b.jpg" is available in "jpg" format from:

<http://arXiv.org/ps/0711.4391v1>

This figure "fig2a.jpg" is available in "jpg" format from:

<http://arXiv.org/ps/0711.4391v1>

This figure "fig2b.jpg" is available in "jpg" format from:

<http://arXiv.org/ps/0711.4391v1>

This figure "fig3.jpg" is available in "jpg" format from:

<http://arXiv.org/ps/0711.4391v1>

This figure "fig4a.jpg" is available in "jpg" format from:

<http://arXiv.org/ps/0711.4391v1>

This figure "fig4b.jpg" is available in "jpg" format from:

<http://arXiv.org/ps/0711.4391v1>

This figure "fig5.jpg" is available in "jpg" format from:

<http://arXiv.org/ps/0711.4391v1>

This figure "fig6.jpg" is available in "jpg" format from:

<http://arXiv.org/ps/0711.4391v1>

This figure "fig7.jpg" is available in "jpg" format from:

<http://arXiv.org/ps/0711.4391v1>

This figure "fig8.jpg" is available in "jpg" format from:

<http://arXiv.org/ps/0711.4391v1>

This figure "fig9.jpg" is available in "jpg" format from:

<http://arXiv.org/ps/0711.4391v1>

This figure "fig10.jpg" is available in "jpg" format from:

<http://arXiv.org/ps/0711.4391v1>